

Learning Noise with Generative Adversarial Networks: Explorations with Classical Random Process Models

Adam Wunderlich and Jack Sklar

Abstract—Random noise arising from physical processes is an inherent characteristic of measurements and a limiting factor for most signal processing tasks. Given the recent interest in generative adversarial networks (GANs) for data-driven signal modeling, it is important to determine to what extent GANs can faithfully reproduce noise in target data sets. In this paper, we present an empirical investigation that aims to shed light on this issue for time series. Namely, we examine the ability of two general-purpose time-series GANs, a direct time-series model and an image-based model using a short-time Fourier transform (STFT) representation, to learn a broad range of noise types commonly encountered in electronics and communication systems: band-limited thermal noise, power law noise, shot noise, and impulsive noise. We find that GANs are capable of learning many noise types, although they predictably struggle when the GAN architecture is not well suited to some aspects of the noise, e.g., impulsive time-series with extreme outliers. Our findings provide insights into the capabilities and potential limitations of current approaches to time-series GANs and highlight areas for further research. In addition, our battery of tests provides a useful benchmark to aid the development of deep generative models for time series.

Index Terms—time series, machine learning, band-limited noise, power law noise, shot noise, impulsive noise, colored noise, fractional Gaussian noise, fractional Brownian motion

I. INTRODUCTION

Noise, commonly defined as an unwanted, irregular disturbance, is a fundamental aspect of all real-world signals that arises from a multitude of natural and man-made sources. Furthermore, the unpredictable, stochastic nature of noise makes it a significant impediment to signal processing and communication. Efforts to understand, mitigate, and harness the effects of noise over the last century have led to the extensive development of many physical and mathematical models, e.g., see [1]–[4] for overviews.

With recent advances in computational hardware and measurement equipment, it is now possible to collect, store, process, and analyze much larger quantities of data than previously possible. Consequently, flexible, data-driven methods for signal modeling and processing are increasingly becoming feasible in many areas of science and engineering [5]. One form of data-driven modeling that has rapidly progressed in recent years is deep generative modeling, a type of unsupervised machine learning that uses deep neural networks to implicitly

represent complicated, high-dimensional data distributions defined by a target training set [6]–[9]. Deep generative models, and most notably, generative adversarial networks (GANs), have been used to successfully synthesize highly-realistic images, audio, video, and text [10]–[13]. Moreover, because deep generative models can learn unknown, unstructured high-dimensional target distributions, they represent a potentially powerful class of methods for many data analysis and signal processing problems [6]–[9].

Since noise is a key component of realistic signals, and given the flourishing interest in GANs in particular, it is important to ask: To what extent are GANs capable of learning various noise types? Answering this question provides insight into potential applications and limitations of GANs and related generative models.

Prior related works include the application of GANs to image denoising [14]–[18], image noise adaption [19], [20], image texture synthesis [21]–[23], and underwater acoustic noise modeling [24]. Although the aforementioned investigations provide some evidence that GANs can learn noise and related distributions, they are limited to particular classes of noise and domain-specific applications. Further, because most prior related studies focus on images, they give little insight into time series, which are of primary interest in many signal processing applications.

The literature on GANs for time series has predominantly focused on audio applications. Many time-series GAN models leverage prior work on GANs for images by training the generator to produce an image-domain, time-frequency representation, such as a spectrogram, which is then mapped into a time series. Models employing this approach include SpecGAN [25], MelGAN [26], TSGAN [27], GANSynth [28], and TiFGAN [29]. Related approaches were compared by Nistal *et al.* [30].

Additionally, there has been some work on GANs that directly model time series. One category of methods includes architectures based on recurrent neural networks [31], [32]. Approaches based on convolutional neural networks include WaveGAN [25], which employs a flattened version of the deep convolutional generative adversarial network (DCGAN) model [33], and QuantGAN [34].

In the present paper, we empirically explore the ability of general-purpose GANs for time series to learn noise modeled as a real-valued, discrete-time random process. Namely, as outlined in Section II, we examine four broad classes of noise commonly encountered in electronics and communication:

A. Wunderlich and J. Sklar are with the Communications Technology Laboratory, National Institute of Standards and Technology, Boulder, Colorado, 80305 USA. e-mail: adam.wunderlich@nist.gov, jack.sklar@nist.gov. U.S. government work not protected by U.S. copyright.

band-limited thermal noise, power law noise, shot noise, and impulsive noise. Within each noise class, we consider multiple random process models over a broad range of parameter values. The mathematical noise models that we consider include stationary, nonstationary, Gaussian, non-Gaussian, and long-memory random processes.

Our evaluations focus on two complementary GAN models for time series based on the popular DCGAN [33] architecture: a direct time-series model, WaveGAN [25], and an image-domain model that uses a complex-valued, short-time Fourier transform (STFT) representation of the time-series [28], [30]. Details are provided in Section III. These GAN architectures were selected for their general-purpose nature, relative simplicity, and straightforward implementation. In a prior investigation, we examined the application of these models to synthetic baseband communication signals [35].

Given the extraordinary number and breadth of noise models [1]–[4] and GAN architectures [10]–[13], it is not feasible to examine all possibilities, and our investigations are necessarily limited in scope. In particular, we do not aim to comprehensively evaluate all published GAN models for time series or to propose a single GAN architecture that works optimally for all noise types. Instead, our goal is to assess the effectiveness of simple, general-purpose, convolutional GAN models for time series. Nonetheless, our empirical studies yield new insights into the capabilities and potential limitations of current approaches to time-series GANs and highlight areas for further research. In addition, our battery of tests provides a useful benchmark to aid future developments.¹

II. NOISE MODELS AND SIMULATION METHODS

In this section, we review the classical noise models and the simulation methods used to generate target distributions for our experiments. Specific parameter choices for our synthetic noise data sets are given in Section VI. Following common practice, unitless quantities are used throughout.

The mathematical models presented here were selected because they cover disparate, well-known noise types and because there are accurate, computationally efficient methods for simulation and parameter estimation. This set of noise models is not comprehensive, and descriptions of additional types of noise can be found in [1]–[4]. For simplicity, we focus on real-valued random processes.

Below, using standard notation, we denote the set of real numbers as \mathbb{R} and the set of integers as \mathbb{Z} . All simulated time series were 4096 samples long, which provided a good balance between realism and computational complexity. Throughout, unitless quantities, e.g., time, are used.

A. Band-Limited Thermal Noise

Thermal noise, also called Johnson-Nyquist noise, arises from the thermal motion of charge carriers inside an electrical conductor [1]–[3]. Thermal noise is commonly modeled as a zero-mean white process, i.e., a sequence of independent,

identically distributed (i.i.d.) random variables with zero mean and finite variance [4], [36]. In the case of radio frequency electronics, thermal noise is band-limited by system components. For this reason, band-limited (or filtered) thermal noise is of interest in many contexts [4], [37].

To simulate band-limited thermal noise, we first generated a white standard normal sequence and then filtered it with a digital bandpass filter. Specifically, we applied a 40th order digital Butterworth filter, implemented using cascaded second-order sections and zero-phase filtering [38]. Frequency responses for the eight bandpass filters used to generate our target distributions are shown in Figure 1.

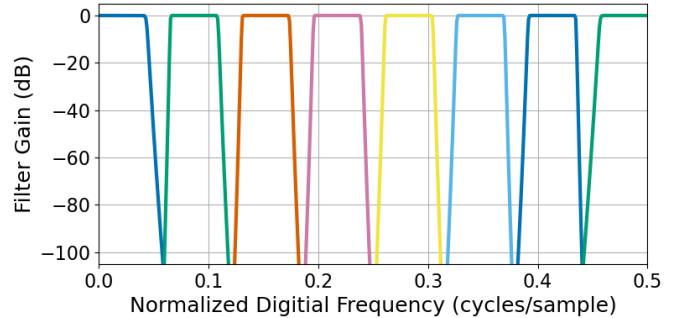


Fig. 1. Frequency response of each digital filter used to simulate band-limited thermal noise.

B. Power Law Noise

Power law noise, also called colored, fractional, or fractal noise, arises in electronics as well as a diverse array of other physical phenomena [1]–[3], [39]. Power law noise is characterized by a power spectral density (PSD), $S(f)$, that is proportional to a power of frequency, f , at low frequencies, i.e., $S(f) \propto |f|^\eta$, where η is a real number. Specific integer powers are often associated with “colors of noise”, e.g., random processes with $\eta = -1, 0,$ and 1 are called pink, white, and blue noise, respectively [40, Ch. 3]. When η is near -1 , the process is also known as $1/f$ noise, flicker noise, or excess noise [2], [39].

We consider three well-studied mathematical models for power law noise: fractionally differenced white noise (FDWN), fractional Gaussian noise (FGN), and fractional Brownian motion (FBM). FDWN and FGN can be interpreted as generalizations of discrete-time white Gaussian noise [41], [42], and FBM can be interpreted as a generalization of the continuous-time Brownian motion (or Wiener) process [42], a commonly-used model for a one-dimensional random walk. The above models arise in the study of self-similar (or fractal) processes, as well as so-called long memory (or persistent) processes. Here, we give a brief overview of FDWN, FGN, and FBM. For additional technical details and properties, see [36], [43], [44].

The stochastic difference equation

$$\nabla^d X_t = \epsilon_t \quad (1)$$

defines a discrete-time FDWN process, X_t . Above, ϵ_t is a zero-mean Gaussian white noise sequence with variance σ_ϵ^2 ,

¹Python software implementing our models and experiments is available at <https://github.com/usnistgov/NoiseGAN>.

and ∇^d is the fractional difference operator defined by the binomial series

$$\nabla^d = (1 - B)^d = \sum_{k=0}^{\infty} \binom{d}{k} (-B)^k, \quad (2)$$

where B is the backward shift operator defined by $BX_t = X_{t-1}$. When the fractional difference parameter, d , is in the open interval $(-0.5, 0.5)$, the FDWN process is stationary with a PSD approximately proportional to $|f|^{-2d}$ as $f \rightarrow 0$ [36], [41], [43].

Another model for power law noise is FGN. FGN is a zero-mean, stationary, discrete-time Gaussian process, Y_t , $t \in \mathbb{Z}$, with autocovariance sequence

$$\text{Cov}(Y_t, Y_{t+k}) = \frac{\sigma_Y^2}{2} (|k-1|^{2H} + |k+1|^{2H} - 2|k|^{2H}), \quad (3)$$

where $k \in \mathbb{Z}$, $\sigma_Y^2 = \text{Var}[Y_t]$, and $H \in (0, 1)$ is called the Hurst index [36], [42], [43]. Note that successive time steps of FGN are negatively correlated when $H \in (0, 0.5)$ and positively correlated when $H \in (0.5, 1)$. In the special case $H = 0.5$, successive time steps are uncorrelated, and FGN reduces to classical white Gaussian noise. Near $f = 0$, the PSD for FGN is proportional to $|f|^{1-2H}$ [36], [42], [44].

FGN arises as the increment process of the continuous-time FBM process, $B_H(t)$, $t \in \mathbb{R}$ [36], [42], [43]. Namely,

$$Y_t = B_H(t+1) - B_H(t), \quad t \in \mathbb{Z}. \quad (4)$$

From the rigorous definition of FBM, e.g., see [42], [43], it follows that $B_H(t)$ is a nonstationary zero-mean Gaussian process with $B_H(0) = 0$ and autocovariance function

$$\text{Cov}[B_h(u), B_h(v)] = \frac{V_H}{2} (|u|^{2H} + |v|^{2H} - |u-v|^{2H}),$$

where $u, v \in \mathbb{R}$, $H \in (0, 1)$, and V_H is a constant that depends on H [43], [45]. In the special case $H = 0.5$, FBM reduces to a classical Brownian motion process [42], [43]. It can be shown that the PSD for FBM is proportional to $|f|^{-(2H+1)}$ [36], [42], [46]; see Flandrin [46] for a rigorous interpretation of the PSD for the nonstationary FBM process.

From the above results, we see that as $f \rightarrow 0$ the PSDs for FDWN and FGN are approximately proportional to $|f|^\eta$, where $\eta \in (-1, 1)$ for $d \in (-0.5, 0.5)$ and $H \in (0, 1)$, respectively. Further, the PSD for FBM is proportional to $|f|^\eta$ where $\eta \in (-3, -1)$ for $H \in (0, 1)$.

As mentioned earlier, the above models exhibit long-range dependence (also called long memory or persistence) in certain cases. Namely, a stationary random process is said to exhibit long-range dependence if its PSD is proportional to $|f|^\eta$ with $\eta \in (-1, 0)$ as $f \rightarrow 0$. Equivalently, a stationary random process has long-range dependence if its autocovariance function is proportional to k^ζ with $\zeta \in (-1, 0)$ as $k \rightarrow \infty$, where $\zeta = -\eta - 1$ [36], [43].

Thus, the stationary FDWN and FGN processes exhibit long-range dependence when $d \in (0, 0.5)$ and $H \in (0.5, 1)$, respectively. Furthermore, since FGN is the increment process of FBM, the increments of FBM have long-range dependence when $H \in (0.5, 1)$. For this reason, the nonstationary FBM

process with $H \in (0.5, 1)$ is sometimes called a nonstationary long memory process.

To produce synthetic FDWN, we used the ‘arfima’ R package [47], which generates a stationary time series with a desired autocovariance function as described in McLeod et al. [48]. To synthesize discrete-time FGN and FBM, we implemented the exact approach of Perrin et al. [49], which utilizes the fast circulant embedding method [50] to generate FGN and applies cumulative summation to obtain discrete-time FBM. All FDWN and FGN simulations set $\sigma_\epsilon^2 = 1$ and $\sigma_Y^2 = 1$.

Examples of FBM time series are shown in Figure 2 for $H = 0.2, 0.5$, and 0.8 . It can be seen that as the Hurst index increases, FBM tends to deviate further from the origin. In Figure 3, Power spectral density (PSD) functions for FDWN, FGN, and FBM are compared for $H = 0.2$ and $H = 0.8$ on a log-log scale. (Note that d and H are related as $d = H - 0.5$.) Here, the PSDs were estimated empirically from a large set of target distribution time series, as described in Section V-A. In addition to the expected slopes for each noise type, one can observe subtle differences in the PSDs for FDWN and FGN.

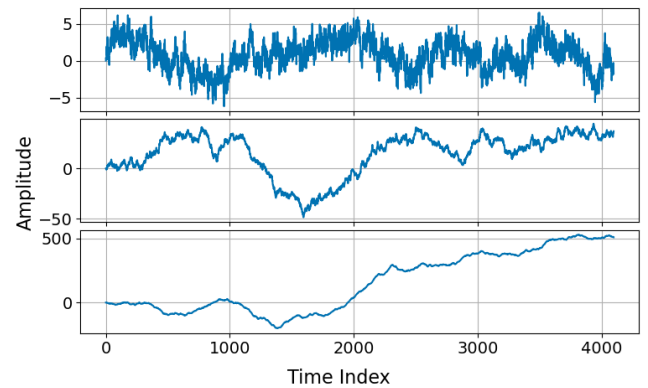


Fig. 2. Example fractional Brownian motion time series with $H = 0.2$ (Top), $H = 0.5$ (Middle), and $H = 0.8$ (Bottom).

C. Shot Noise

Shot noise, also called Poisson noise or photon noise, arises from the random arrival of discrete charge carriers in electronics and photons in optics [1]–[4]. Shot noise can be modeled using a filtered Poisson process of the form

$$X(t) = \sum_{n=1}^{N(t)} A_n p(t - \tau_n), \quad t > 0, \quad (5)$$

where $N(t)$, the number of events in the interval $(0, t]$, is a homogeneous Poisson point process with event rate ν and event times, $\{\tau_n\}$ [3], [4], [51]–[53]. If $N(t) = 0$, then the sum is taken to be zero. Above, $p(t)$ is a deterministic pulse function, and the pulse amplitudes, $\{A_n\}$, are independent, identically distributed, and independent of $N(t)$. For a finite time interval of length T , the number of events, N is Poisson distributed with mean νT , and the event times, $\{\tau_1, \tau_2, \dots, \tau_N\}$, are uniformly distributed on the interval [51, p. 140].

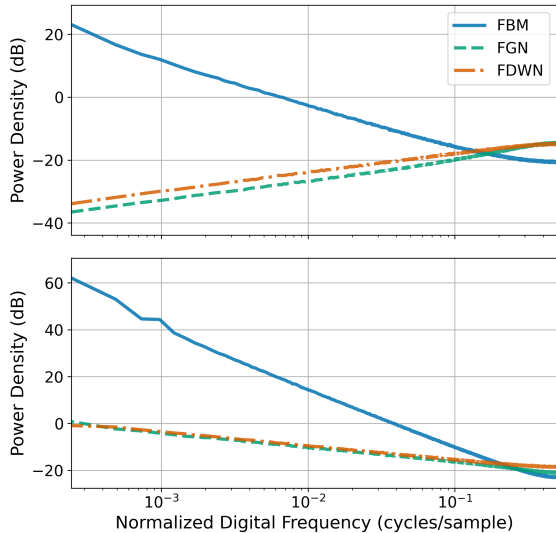


Fig. 3. Comparison of estimated Power Spectral Density functions on a log-log scale for each of the power law noise types with $H = 0.2$ (Top) and $H = 0.8$ (Bottom).

Following Theodorsen et al. [53], we assumed that the pulse amplitudes follow an exponential distribution with mean β . Also, we considered the three pulse functions listed in Table I, which were taken from Howard [4, p. 506], where $u(t)$ denotes the unit step function equal to one for $t \geq 0$ and zero otherwise, and σ_d is a pulse duration parameter. Note that the three pulse functions are ordered from top to bottom with respect to increasing smoothness. Table I also lists the integrals $I_1 = \int_{-\infty}^{\infty} p(t) dt$ and $I_2 = \int_{-\infty}^{\infty} p(t)^2 dt$ of each pulse function, which are used for the event rate estimator introduced in Section V-B.

For a finite time interval, $(0, T]$, the mean and autocovariance of the shot noise process are time-dependent, approaching steady-state values as $t, T \rightarrow \infty$ [4]. Therefore, to approximate a weak-sense stationary discrete-time shot noise process, we generated a length $2L$ process of duration $T = (2L - 1)\Delta t \gg \sigma_d$ and then discarded the first L samples. Namely, defining a discrete-time grid $t_m = m\Delta t$, for $m = 0, 1, \dots, 2L - 1$, we drew N from a Poisson distribution with mean νT , where $T = (2L - 1)\Delta t$. Next, we randomly generated N integers $\{m_1, m_2, \dots, m_N\}$ from a discrete uniform distribution on $[0, 2L - 1]$ and drew $\{A_1, A_2, \dots, A_N\}$ independently from an exponential distribution with mean β . Then, we formed the impulse sequence

$$f[m] = \sum_{n=1}^N A_n \delta_{m, m_n}, \quad (6)$$

where δ_{m, m_n} is a Kronecker delta function, and performed the discrete convolution of $f[m]$ with the sampled pulse function, $p(t_m)$, retaining the $2L$ samples in the middle of the convolution result. Last, we discarded the first L samples to remove any transients and approximate a steady-state realization of a length L discrete-time shot noise process. The validity of the steady-state simulated shot noise time series was verified by checking that there was close agreement between the em-

TABLE I
PULSE FUNCTIONS USED TO SIMULATE SYNTHETIC SHOT NOISE.

Pulse Type	$p(t)$	I_1	I_2
One-sided Exponential	$\frac{1}{\sigma_d} \exp[-t/\sigma_d]u(t)$	1	$\frac{1}{2\sigma_d}$
Linear Exponential	$\frac{t}{\sigma_d^2} \exp[-t/\sigma_d]u(t)$	1	$\frac{1}{4\sigma_d}$
Gaussian	$\frac{1}{\sigma_d\sqrt{2\pi}} \exp[-t^2/(2\sigma_d^2)]$	1	$\frac{1}{2\sigma_d\sqrt{\pi}}$

pirical autocovariance function and the theoretical asymptotic autocovariance function [4].

For all shot noise simulations, we set $\sigma_d = 1$, $\beta = 1$, and $\Delta t = 0.1$. Example synthetic shot noise time series with a one-sided exponential pulse function and event rates $\nu = 0.25$, 0.5, and 2 are shown in Figure 4. A comparison of PSDs for different pulse types with $\nu = 1$ is given in Figure 5; the PSDs were estimated empirically as described in Section V-A. For different event rates, ν , the PSDs have the same shape and are simply shifted vertically by a factor proportional to ν [4].

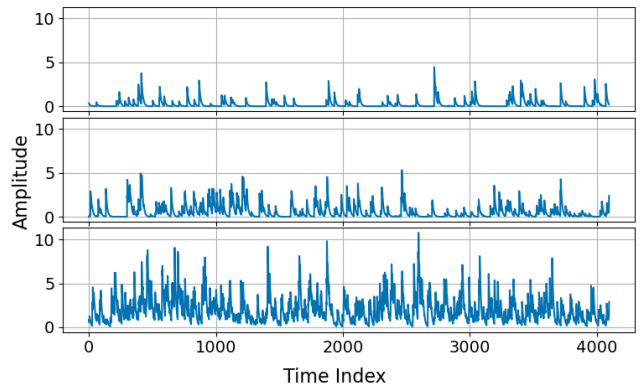


Fig. 4. Example shot noise time series with one-sided exponential pulse type and event rates $\nu = 0.25$ (Top), $\nu = 0.5$ (Middle), and $\nu = 2$ (Bottom).

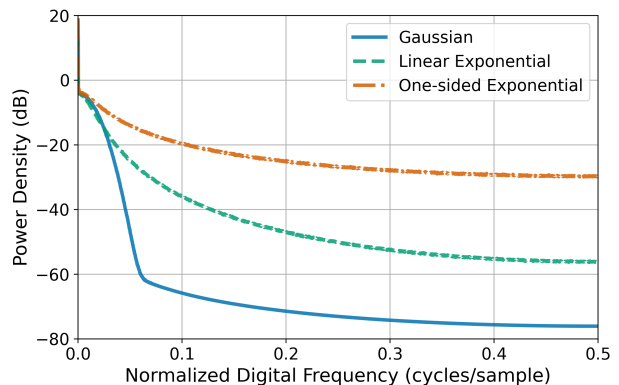


Fig. 5. Comparison of shot noise power spectral density functions for different pulse types with $\nu = 1$. Note that all curves are shifted vertically by a constant factor for different event rates, ν .

D. Impulsive Noise

Impulsive noise, consisting of random, large bursts of short duration arising from either naturally occurring or man-made

sources, is a limiting factor for many communication scenarios [54]–[57], including wireless [58], [59], digital subscriber line [60], [61], power line [62], [63], and undersea acoustic environments [64], [65]. Many models for impulsive noise have been developed; see Shongwe et al. [66] for an overview. We focused on two well-studied impulsive noise models that were straightforward to implement and evaluate: the Bernoulli-Gaussian and symmetric alpha-stable models, described below. These models both define non-Gaussian, memoryless, white processes with a power spectrum that is constant across all frequencies. Impulse noise models with memory have also been proposed, e.g., see [63], [66], but such models are outside the scope of the present study.

A simple impulsive noise model that has been applied in many contexts is the Bernoulli-Gaussian (BG) model [54], [56], [57], [63], independently defined at each discrete time step as

$$X_{BG} = N_w + BN_i, \quad (7)$$

where N_w and N_i are independent, zero-mean, normal random variables with variances σ_w^2 and σ_i^2 , respectively, and B is a Bernoulli random variable with mean p , i.e., the probability that $B = 1$ is p , where p is called the impulse probability. Above, N_w corresponds to a thermal noise background and N_i is intermittent impulsive noise. The probability density function (PDF) for X_{BG} is the Gaussian mixture

$$f(x) = (1 - p)\mathcal{N}(x; 0, \sigma_w^2) + p\mathcal{N}(x; 0, \sigma_w^2 + \sigma_i^2) \quad (8)$$

where $\mathcal{N}(x; \mu, \sigma^2)$ denotes the PDF for a normal distribution with mean μ and variance σ^2 .

We simulated independent BG noise at each time step using equation (7) with $\sigma_w = 0.1$ and $\sigma_i = 1$. Example time series are shown in Figure 6 for $p = 0.01$, 0.05, and 0.1. Corresponding PDFs are plotted on a logarithmic scale on the left side of Figure 8.

Another popular model for impulsive noise in signal processing and communications is the symmetric α -stable ($S\alpha S$) family of distributions, a subclass of the stable (a.k.a. Levy α -stable) family of distributions, which are used to model heavy-tailed, non-Gaussian phenomena [55], [67]–[70]. The PDF of a $S\alpha S$ distribution can be succinctly expressed in terms of its characteristic function as

$$f(x; \alpha, \gamma, \delta) = \frac{1}{2\pi} \int_{-\infty}^{\infty} \exp(i\delta u - \gamma|u|^\alpha) e^{-iu x} du, \quad (9)$$

where $i^2 = -1$, $\alpha \in (0, 2]$ is the characteristic exponent, $\gamma > 0$ is the scale parameter, and $\delta \in \mathbb{R}$ is the location parameter.² A $S\alpha S$ distribution is said to be “standard” if $\delta = 0$ and $\gamma = 1$. The special cases $\alpha = 1$ and $\alpha = 2$ correspond to Cauchy and normal distributions, respectively. As α decreases, the PDF has a sharper peak and the tails become heavier [67], [68].

We considered discrete time $S\alpha S$ processes where the value at each time step is an independent standard $S\alpha S$ random variable with parameter α . To simulate standard $S\alpha S$ variates, we used the ‘pylevy’ Python module [71], which implements a

²Many different parameterizations for stable distributions are in use; see Nolan [67, Secs. 1.3, 3.5] for an overview. Here, we used the parameterization of Nikias and Shao [68].

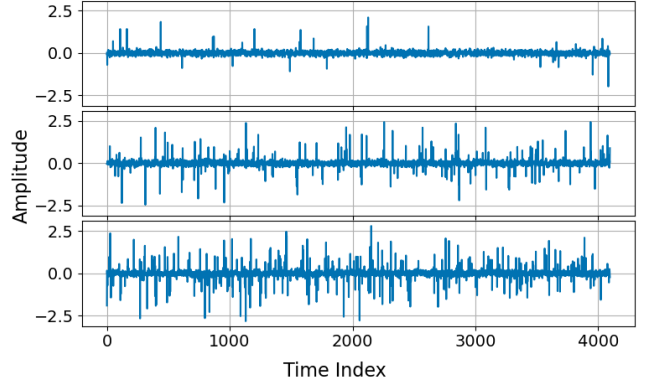


Fig. 6. Example Bernoulli-Gaussian time series with $\sigma_w = 0.1$ and $\sigma_i = 1$ for $p = 0.01$ (Top), $p = 0.05$ (Middle), and $p = 0.1$ (Bottom).

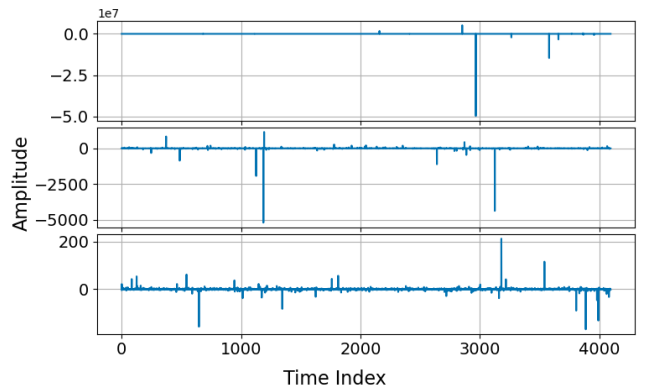


Fig. 7. Example time series with a standard symmetric α -stable distribution. Top: $\alpha = 0.5$, Middle: $\alpha = 1$, Bottom: $\alpha = 1.5$.

method of Chambers et al. [72] for generating stable random variables; see also [67]. Example time series are shown in Figure 7 for three values of α . Corresponding PDFs are plotted on a logarithmic scale on the right side of Figure 8.

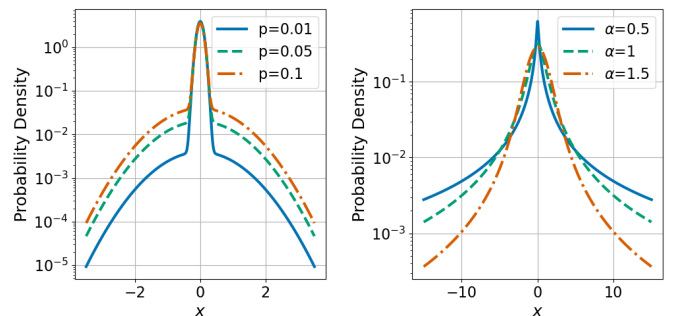


Fig. 8. Example probability density functions for impulsive noise. Left: Bernoulli-Gaussian with $\sigma_w = 0.1$ and $\sigma_i = 1$. Right: standard symmetric α -stable.

Comparing the example time series plots in Figure 6 and Figure 7, we see that the range of BG noise is fairly consistent across different impulse probabilities, p . On the other hand, the range of $S\alpha S$ noise varies by several orders of magnitude for different values of the characteristic exponent, α . These ob-

servations are consistent with the corresponding PDFs shown in Figure 8. Namely, because BG noise is a mixture of two Gaussian distributions, BG noise has rapidly decaying “light” tails, whereas $S\alpha S$ noise has slowly decaying “heavy” tails with a higher probability of extreme values [73].

III. GAN MODELS

We implemented two CNN-based GAN models for our experiments that are based on the widely used DCGAN model [33]: a 1-D convolutional model trained directly on time series, called WaveGAN [25] and a 2-D convolutional model trained on the complex valued STFT of the waveforms [28], [30]. Both models were designed to generate time series of length 4096. Details on these models are given below. Familiarity with deep learning and GANs is assumed; for introductions to these topics, see, e.g., the textbooks [6], [7], [74], [75].

A. WaveGAN

The original WaveGAN model produced single-channel audio waveforms of length 16 384, using an architecture based on a 1-D flattened version of the popular DCGAN model for images [33]. WaveGAN widened its convolutional receptive field by modifying the DCGAN 5x5 kernels with 2x2 strides to 1-D kernels of length 25 with strides of 4 [25]. Also, in contrast to DCGAN, WaveGAN had no normalization layers and added a fully connected layer to both models.

In addition, WaveGAN performs a so-called “phase-shuffle” operation, consisting of a random circular shift, on the activation output of each convolutional layer in the discriminator. Our implementation applied a random circular shift between -2 and 2 time steps, which Donahue *et al.* [25] found to be an optimal range.

Tables II and III outline our slightly modified architectures for the WaveGAN generator and discriminator, respectively. Like the original WaveGAN model, our implementation uses five convolutional layers for the generator and discriminator, but the dense layer is modified to support the 4096 length of our synthetic noise waveforms. In these tables, Dense, Conv 1-D and Transpose Conv 1-D, denote dense fully connected layers, one-dimensional convolutional layers, and transposed convolutional layers, respectively. Also, Tanh, ReLU, and LReLU indicate hyperbolic-tangent (Tanh), rectified linear unit (ReLU), and leaky rectified linear unit (LReLU) activation functions. The filter dimensions for convolutional layers correspond to kernel length, number of input channels, and number of output channels, respectively. Similarly, the filter dimensions for the dense layers correspond to input length and output length, respectively. The first output shape dimension, n , denotes the batch size.

B. Short-Time Fourier Transform GAN (STFT-GAN)

GANs based on STFT representations have been proposed for audio generation, e.g., see [28], [30]. Here, we used a similar model, denoted STFT-GAN, that was based on the DCGAN architecture [33].

The discrete STFT for a real-valued time series is computed by dividing the time series into overlapping segments of equal

TABLE II
WAVEGAN GENERATOR ARCHITECTURE.

Operation	Filter Shape	Output Shape
$z \sim \text{Uniform}(-1, 1)$		$(n, 100)$
Dense	$(100, 4096)$	$(n, 4096)$
Reshape		$(n, 1024, 4)$
ReLU		$(n, 1024, 4)$
Transpose Conv1-D (stride=4)	$(25, 1024, 512)$	$(n, 512, 16)$
ReLU		$(n, 512, 16)$
Transpose Conv1-D (stride=4)	$(25, 512, 256)$	$(n, 256, 64)$
ReLU		$(n, 256, 64)$
Transpose Conv1-D (stride=4)	$(25, 256, 128)$	$(n, 128, 256)$
ReLU		$(n, 128, 256)$
Transpose Conv1-D (stride=4)	$(25, 128, 64)$	$(n, 64, 1024)$
ReLU		$(n, 64, 1024)$
Transpose Conv1-D (stride=4)	$(25, 64, 2)$	$(n, 1, 4096)$
Tanh		$(n, 1, 4096)$

TABLE III
WAVEGAN DISCRIMINATOR ARCHITECTURE.

Operation	Filter Shape	Output Shape
$x \sim G(z)$		$(n, 1, 4096)$
Conv1-D (stride=4)	$(25, 2, 64)$	$(n, 64, 1024)$
LReLU($\alpha = 0.2$)		$(n, 64, 1024)$
Conv1-D (stride=4)	$(25, 64, 128)$	$(n, 128, 256)$
LReLU($\alpha = 0.2$)		$(n, 128, 256)$
Conv1-D (stride=4)	$(25, 128, 256)$	$(n, 256, 64)$
LReLU($\alpha = 0.2$)		$(n, 256, 64)$
Conv1-D (stride=4)	$(25, 256, 512)$	$(n, 512, 16)$
LReLU($\alpha = 0.2$)		$(n, 512, 16)$
Conv1-D (stride=4)	$(25, 512, 1024)$	$(n, 1024, 4)$
LReLU($\alpha = 0.2$)		$(n, 1024, 4)$
Reshape		$(n, 4096)$
Dense	$(1024, 1)$	$(n, 1)$

length, applying a window function, and then calculating the one-sided discrete Fourier transform (DFT) on each segment [76], [77]. Unless stated otherwise, we used a Hann window of length 128 with 50% segment overlap, which for a 4096 length time series produces a (one-sided) STFT with dimensions of 65×65 . In this case, the constant-overlap-add (COLA) constraint is satisfied, and the STFT can be inverted to obtain a time series of the original length [76]. The two channels of the discrete STFT correspond to the real and imaginary parts of the complex-valued STFT.

STFT-GAN is composed of five 2-D convolutional layers with 4×4 kernels for both the generator and discriminator; see Tables IV and V. In the tables, the notation is similar to that used for WaveGAN, with Conv 2-D and Transpose Conv 2-D indicating two-dimensional convolutional and transposed convolutional layers, and n denoting the batch size.

IV. TRAINING AND IMPLEMENTATION

A. Baseline Implementation

Following the original WaveGAN training implementation [25], both models were trained using Wasserstein GAN loss with gradient penalty (WGAN-GP) [78], and the ADAM optimizer [79], with WaveGAN using hyperparameter settings of $\alpha = 10^{-4}$, $\beta_1 = 0.5$, and $\beta_2 = 0.9$ for the learning rate and moment decay rates, respectively. STFT-GAN differs by setting $\beta_1 = 0$, which was recommended in [78]. WaveGAN is trained with a 5:1 update ratio between the generator and discriminator, while STFT-GAN uses a 1:1 update ratio, which

TABLE IV
STFT-GAN GENERATOR ARCHITECTURE

Operation	Filter Shape	Output Shape
$z \sim \text{Uniform}(-1, 1)$		$(n, 100)$
Dense	(100, 4096)	$(n, 4096)$
Reshape		$(n, 1024, 2, 2)$
ReLU		$(n, 1024, 2, 2)$
Transpose Conv2-D (stride=2)	(4, 4, 1024, 512)	$(n, 512, 4, 4)$
ReLU		$(n, 512, 4, 4)$
Transpose Conv2-D (stride=2)	(4, 4, 512, 256)	$(n, 256, 8, 8)$
ReLU		$(n, 256, 8, 8)$
Transpose Conv2-D (stride=2)	(4, 4, 256, 128)	$(n, 128, 16, 16)$
ReLU		$(n, 128, 16, 16)$
Transpose Conv2-D (stride=2)	(4, 4, 128, 64)	$(n, 64, 32, 32)$
ReLU		$(n, 128, 32, 32)$
Transpose Conv2-D (stride=2)	(4, 4, 64, 2)	$(n, 2, 65, 65)$
Tanh		$(n, 2, 65, 65)$

TABLE V
STFT-GAN DISCRIMINATOR ARCHITECTURE

Operation	Filter Size	Output Shape
$x \sim \mathcal{G}(z)$		$(n, 2, 65, 65)$
Conv2-D (stride=2)	(4, 4, 2, 64)	$(n, 64, 32, 32)$
LReLU($\alpha = 0.2$)		$(n, 64, 32, 32)$
Conv2-D (stride=2)	(4, 4, 64, 128)	$(n, 128, 16, 16)$
LReLU($\alpha = 0.2$)		$(n, 128, 16, 16)$
Conv2-D (stride=2)	(4, 4, 128, 256)	$(n, 256, 8, 8)$
LReLU($\alpha = 0.2$)		$(n, 256, 8, 8)$
Conv2-D (stride=2)	(4, 4, 256, 512)	$(n, 512, 4, 4)$
LReLU($\alpha = 0.2$)		$(n, 512, 4, 4)$
Conv2-D (stride=2)	(4, 4, 512, 1024)	$(n, 1024, 2, 2)$
LReLU($\alpha = 0.2$)		$(n, 1024, 2, 2)$
Reshape		$(n, 4096)$
Dense	(4096, 1)	$(n, 1)$

we found to yield better convergence on target data sets in preliminary testing.

We trained each model with a target data set of size $2^{14} = 16\,384$, for 500 epochs with a batch size of 128. Prior to training, all target data sets were scaled using feature min-max scaling, which scales each feature to the interval $[-1, 1]$, corresponding to the range of the tanh output activation of the generator [33]. All outputs from the generator were rescaled back to the original range using the corresponding inverse scaling transformation.

B. Quantile Data Transformation for Impulsive Noise

As we will see later, the impulsive noise types were particularly challenging for our baseline GAN models. Consequently, for the impulsive noise types, we also investigated replacing the feature min-max scaling of the target data with a quantile transformation [80, Sec. 7.4.1] applied independently to each channel to make the data approximately follow a standard normal distribution. The motivations for this transformation were twofold: (1) it ensured that the distribution of each channel was unimodal with “light” tails [73], and (2) it effectively limited the impact of outliers.

We implemented the quantile transformation using the “quantile_transform” method in the scikit-learn Python library [81]. This method is based on the formula $Y = F_Y^{-1}(F_X(X))$, where X is an input random variable with continuous cumulative distribution function (CDF) $F_X(x)$, and Y is an output random variable with desired continuous CDF $F_Y(y)$. In our

case, $F_Y(y)$ is the CDF for a standard normal distribution. The transformation formula follows from the fact that the random variable $F_X(X)$ has a uniform distribution on the interval $[0, 1]$ [80, Sec. 7.4.1]. In practice, to apply this method to a sample of X , F_X is replaced by the empirical CDF.

The quantile transformation for a given training set was estimated using 1024 uniformly-spaced quantiles for each target distribution channel. Any data values that exceed the most extreme quantiles were clipped to those values. For WaveGAN, the transformation was fit directly to the time series values, whereas for STFT-GAN, the transformation was fit on the real and imaginary channels of the target STFT distribution separately. For both models, a scaled-tanh activation was used at the end of the generator to limit the absolute-maximum value of generated data to the absolute maximum of the target quantile-transformed distribution. Finally, the inverse quantile transformation was applied to each channel of the generated data to return it to the original range.

While the quantile transformation method is included in the commonly used scikit-learn Python library, to our knowledge, it has not been previously proposed as a preprocessing step for GAN training.

V. EVALUATION METHODS

Our evaluations focused on power spectral density (PSD) and characteristic parameters for each noise type. Evaluations for each noise type with fixed parameter values were conducted using independent target test sets of size 4096.

A. Power Spectral Density (PSD) Assessment

The PSD for each time series was estimated with the multitaper method, a versatile nonparametric approach [82], [83]. Specifically, we used the implementation in the Python ‘Spectrum’ package [84] with the time half-bandwidth parameter set to $NW = 4$, the first $k = 7$ Slepian sequences, the FFT length set to 4096, and the fast ‘eigen’ method for result weighting. These parameter choices are typical and were found to yield consistent results. To obtain a representative PSD estimate across a test set, we first applied the multitaper method to each time series and then calculated the median value in each frequency bin. The uncertainties in the median PSD estimate across the test set were negligible in the context of our evaluations. This procedure was carried out on both target and generated distributions across all noise types.

Denote the one-sided median PSDs for the target and generated distributions as $P_t(f_d)$ and $P_g(f_d)$, respectively, where $f_d \in [0, 0.5]$ is normalized digital frequency with units of cycles per sample. To assess the accuracy of P_g relative to P_t , we used a one-sided version of Georgiou’s “geodesic distance” for power spectra [85], defined as³

$$d_g(P_g, P_t) = \sqrt{\int_0^{0.5} \left(\log \frac{P_g(f_d)}{P_t(f_d)} \right)^2 \frac{df_d}{0.5} - \left(\int_0^{0.5} \log \frac{P_g(f_d)}{P_t(f_d)} \frac{df_d}{0.5} \right)^2}. \quad (10)$$

³Consistent with Georgiou’s definition, the integrals were normalized by the length of the integration interval.

The above distance can be interpreted as the length of a geodesic connecting points on a manifold of PSDs [86]. Moreover, it does not distinguish PSDs that differ by a constant, positive factor, i.e., $d_g(P_g, P_t) = d_g(P_g, \kappa P_t)$ for any $\kappa > 0$ [85]. Because the first term depends on the difference of log-transformed power spectra, it has the desirable property of reflecting differences in areas of both low and high power spectral density.

To estimate the geodesic PSD distance, we first estimated discrete one-sided PSDs, $P_g[k]$ and $P_t[k]$, on the discrete digital frequency grid $f_d^k = k\Delta f_d$, where $k = 0, \dots, N-1$, $\Delta f_d = 0.5/N$, and $N = 4096$. Approximating the integrals in Eq.(10) with summations, yields

$$d_g(P_g, P_t) \approx \sqrt{\sum_{k=0}^N \left(\log \frac{P_g[k]}{P_t[k]} \right)^2 \frac{\Delta f_d}{0.5} - \left(\sum_{l=0}^N \log \frac{P_g[l]}{P_t[l]} \frac{\Delta f_d}{0.5} \right)^2}. \quad (11)$$

We implemented the above formula with a natural logarithm, but the choice of logarithm is arbitrary.

B. Noise Model Parameters

For each noise type, except for band-limited thermal noise, we assessed how well the generated time series distribution matched the target distribution in terms of characteristic noise parameters. The specific noise parameter estimation procedures are described below. Later, boxplots are used to compare distributions of estimated noise parameters for target and generated time series distributions. Boxplots of parameter estimates for target distributions capture the inherent bias and variability of the parameter estimators described below and hence provide a basis for assessing the estimated parameter distributions for the generated data.

For power law noise distributions, we evaluated the accuracy of the recovered fractional difference parameter, d , for FDWN as well as the Hurst index, H , for FGN and FBM. The fractional difference parameter for FDWN was estimated using a maximum likelihood fitting method implemented in the ‘arfima’ R package [44], [47]. The Hurst index for FGN and FBM is estimated using the “discrete variations” method [87]–[89] implemented with a second-order difference filter.

Under the assumption that the shot noise pulse amplitudes follow an exponential distribution, which is true for our target distributions, we assessed the shot noise event rate, ν , using the (apparently novel) estimator

$$\hat{\nu} = \frac{2\hat{\mu}_X^2 I_2}{\hat{\sigma}_X^2 I_1^2}, \quad (12)$$

where $\hat{\mu}_X$ and $\hat{\sigma}_X^2$ are the estimated mean and variance of the shot noise time series, and where $I_1 = \int_{-\infty}^{\infty} p(t) dt$ and $I_2 = \int_{-\infty}^{\infty} p(t)^2 dt$ are integrals of the known pulse function, $p(t)$; see Table I. A derivation of the above estimator is given in the Appendix.

For each of the impulsive noise models, we evaluated two characteristic parameters. Namely, for BG noise, we assessed the impulse probability, p , and the scale parameter ratio, $\theta = \sqrt{\sigma_w^2 + \sigma_i^2}/\sigma_w$, which measures the relative dispersion of

the mixture components; see equation (8). The BG parameters were estimated by fitting a two-component Gaussian mixture model using the iterative expectation maximization method implemented in the scikit-learn Python library [81]. To assess $S\alpha S$ noise, we estimated the characteristic exponent, α , and the scale parameter, γ , using the “fast” methods of Tsihrintzis and Nikias [90].

VI. EXPERIMENTAL RESULTS

A. Band-limited Thermal Noise

The eight digital bandpass filters shown in Figure 1 were used to simulate eight target data sets of band-limited thermal noise, where each data set contained noise limited to a single band. Estimated geodesic PSD distance between the target and generated distributions is plotted in Figure 9 (Top), where the bands are ordered in terms of increasing center frequency. It is evident that STFT-GAN yielded uniformly better PSD fidelity than WaveGAN. To gain more insight, median estimated PSDs for band number 3 are shown in Figure 9 (Bottom); other bands are similar. We see that STFT-GAN more closely tracked the target PSD out-of-band, whereas WaveGAN suffered from a limited dynamic range.

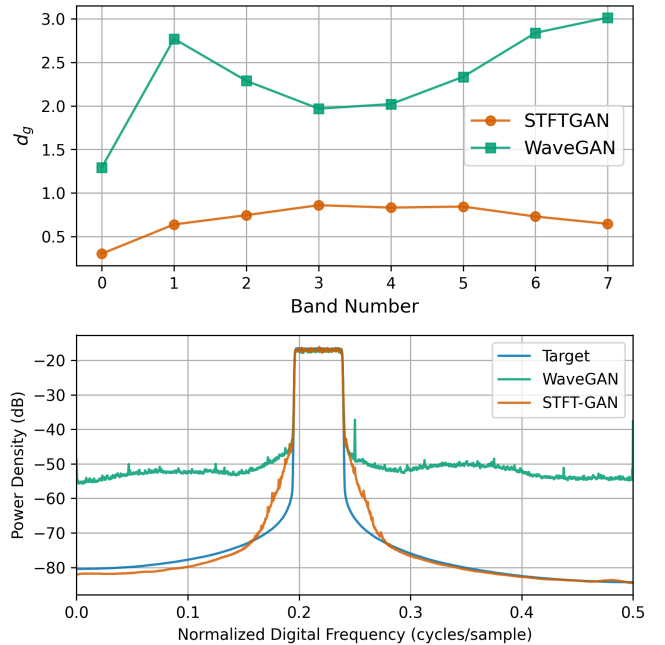


Fig. 9. Results for band-limited thermal noise. Top: Geodesic PSD distance results. Bottom: Median PSD comparison for band #3.

B. Power Law Noise

Target distributions defined by the three power law noise models from Section II-B were evaluated for $H = 0.05, 0.1, 0.2, 0.3, 0.4, 0.5, 0.6, 0.7, 0.8, 0.9$, and 0.95 . (Recall that $d = H - 0.5$.) PSD distance results and boxplots of estimated fractional noise parameters are given in Figure 10 for FGN and FDWN. The plots show that STFT-GAN learned these processes accurately. However, WaveGAN did not reproduce

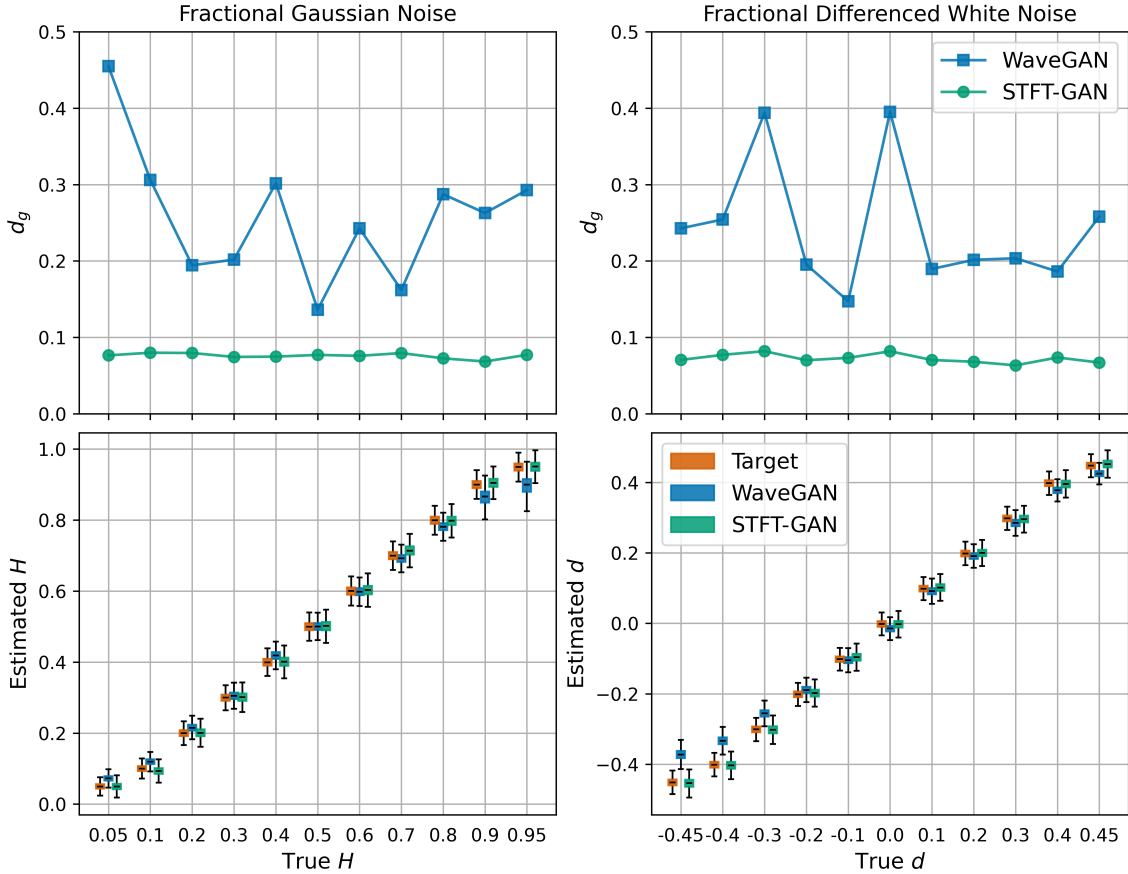


Fig. 10. Aggregate results for FGN and FDWN. Top: Geodesic PSD distance plots. Bottom: Estimated fractional parameter boxplots.

the target distributions as well, especially at the extremes of the parameter range.

Results for FBM are shown in Figure 11. In addition to the baseline 65×65 STFT size, we also tested STFT-GAN with an STFT dimension of 129×65 , resulting from a window segment length of 256 with 75% overlap. We denote the baseline and modified models as STFT-GAN (65×65) and STFT-GAN (129×65), respectively. The modified model, STFT-GAN (129×65), which had higher frequency resolution than the baseline model, accurately learned FBM over the full parameter range and achieved excellent PSD fidelity across all frequencies, as shown in Figure 12 for $H = 0.8$. By contrast, both WaveGAN and STFT-GAN (65×65) failed to accurately recover the target PSD and target Hurst index across the full parameter range, with the WaveGAN model failing at lower Hurst indices than STFT-GAN.

C. Shot Noise

Target distributions defined by the shot noise model described in Section II-C were assessed with the three pulse types in Table I for the event rates $\nu = 0.25, 0.5, 0.75, 1.0, 1.25, 1.5, 1.75, 2.0, 2.25, 2.5, 2.75,$ and 3.0 . Figure 13 contains the PSD distance results and estimated event rate boxplots. The PSD distance results indicate that WaveGAN had worse PSD fidelity as the pulse type grew smoother.

Namely, while WaveGAN was able to learn the PSD well for one-sided exponential shot noise, it performed worse for linear exponential and Gaussian pulses. By contrast, STFT GAN was fairly robust to pulse smoothness, resulting in excellent PSD fidelity over the full range of event rates for each pulse type.

Figure 14 compares median PSDs for the one-sided exponential and Gaussian pulse types when the target event rate is $\nu = 1$. These plots demonstrate that while WaveGAN accurately recovered the PSD for the one-sided exponential pulse type, it failed to capture the faster decay of the PSD for the Gaussian pulse type. Contrastly, STFT-GAN achieved excellent PSD fidelity for both pulse types.

Representative example target and generated time series for one-sided exponential shot noise for a target event rate of $\nu = 0.25$ are plotted in Figure 15. From this figure, it can be seen that WaveGAN correctly learned to generate non-negative shot noise time series, while STFT-GAN generated time series with occasional small negative values.

D. Impulsive Noise

Last, the ability of the two GAN models to learn impulsive noise defined by the BG and $S\alpha S$ models described in Section II-D was evaluated. Specifically, BG noise with $\sigma_w = 0.1$ and $\sigma_i = 1$, i.e., a scale parameter ratio of $\theta = \sqrt{\sigma_w^2 + \sigma_i^2}/\sigma_w \approx 10.05$, was assessed for impulse probabilities of $p = 0.01, 0.05, 0.1, 0.15, 0.2, 0.3, 0.4, 0.5, 0.6,$

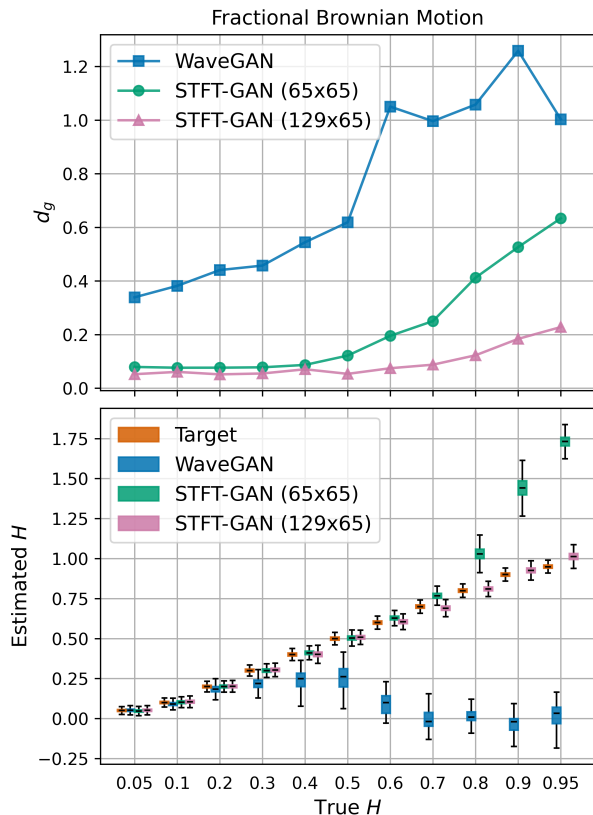


Fig. 11. Aggregate results for Fractional Brownian Motion. Top: Geodesic PSD distance plots. Bottom: Boxplots of estimated Hurst index.

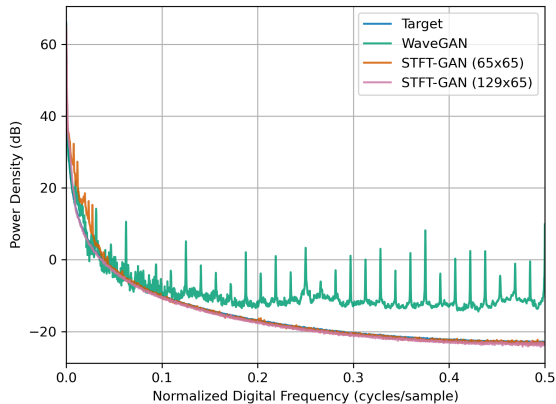


Fig. 12. Median PSD comparisons for FBM with $H = 0.8$.

0.7, 0.8, and 0.9. Standard $S\alpha S$ noise with location and scale parameters equal to zero and one, respectively, was evaluated for characteristic exponents $\alpha = 0.5, 0.6, 0.7, 0.8, 0.9, 1.0, 1.1, 1.2, 1.3, 1.4$, and 1.5 . As described in Section IV, the WaveGAN and STFT-GAN models were trained with the two different preprocessing schemes described in Section IV: (1) a baseline implementation using feature min-max scaling and (2) an implementation applying a quantile data transformation, which transforms each channel to an approximate standard normal distribution.

Figure 16 presents the aggregate results for Bernoulli-

Gaussian noise. From the top row, we see that the PSD fidelity as measured by geodesic distance was excellent for STFT-GAN with both preprocessing schemes, but that WaveGAN required the quantile transformation to recover the PSD accurately. The boxplots for estimated impulse probability in the middle row and estimated scale ratio in the bottom row demonstrate that STFT-GAN often failed to accurately learn both distribution parameters. WaveGAN with the baseline implementation successfully recovered the impulse probability for $p \leq 0.6$, although it did not learn the correct scale ratio in most cases. By contrast, WaveGAN with the quantile transformation accurately recovered the target impulse probability and scale ratio across most scenarios, except for the extreme $p = 0.01$ and $p = 0.9$ cases.

Example target and generated time series for GANs with the quantile data transformation are shown in Figure 17 for the case of $p = 0.05$ BG noise. From these plots, it is evident that STFT-GAN failed to recover the correct background noise level relative to the impulsive component, while WaveGAN better matched the target distribution.

In the $S\alpha S$ noise tests, the GAN models without quantile transformation suffered from mode-collapse during training. Specifically, WaveGAN and STFT-GAN generated time series with extreme impulses at the same time indices, exhibiting very little diversity. For this reason, results for the models without quantile transformation are not presented.

By contrast, the quantile data transformation preprocessing step enabled both GAN models to avoid mode-collapse during training. Aggregate results for the GANs with quantile transformation are given in Figure 18. We see that WaveGAN exhibited excellent PSD fidelity and accurately recovered the target scale parameter, whereas STFT-GAN did not. On the other hand, both GAN models failed to accurately learn the target characteristic exponent.

Example target and generated time series for GANs trained with a quantile data transformation on $S\alpha S$ noise with $\alpha = 1.0$ are shown in Figure 19. From these plots, we see that WaveGAN produced short-duration impulses, whereas STFT-GAN produced impulses that were not as localized in time. These observations are consistent with the PSD results. Both models often produced time series with maximum impulse amplitudes that were too large, supporting the finding that they did not consistently recover the target characteristic exponent.

VII. DISCUSSION AND CONCLUSIONS

We examined the ability of two general-purpose GAN models for time series, WaveGAN and STFT-GAN, to faithfully learn several types of noise that frequently arise in communications and signal processing. Specifically, we investigated four classes of noise with well-established models: band-limited thermal noise, power law noise, shot noise, and impulsive noise. In addition, within each noise class, we considered multiple types over a broad range of parameter values. Performance evaluations focused on PSD fidelity as well as recovery of characteristic parameters associated with each random process model.

In many cases, both the time-domain WaveGAN model and the image-domain STFT-GAN model successfully recovered

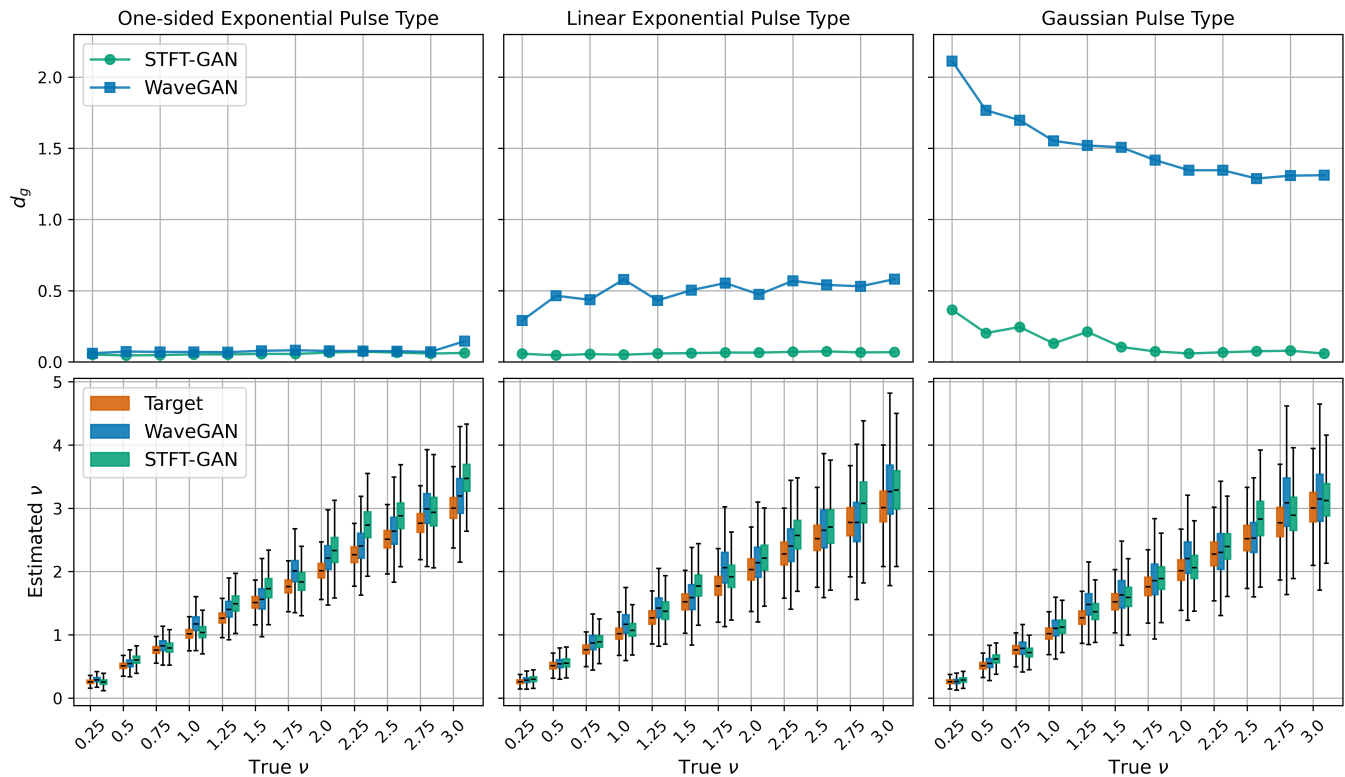


Fig. 13. Shot noise results. Top: Geodesic PSD distance plots. Bottom: Estimated event rate boxplots.

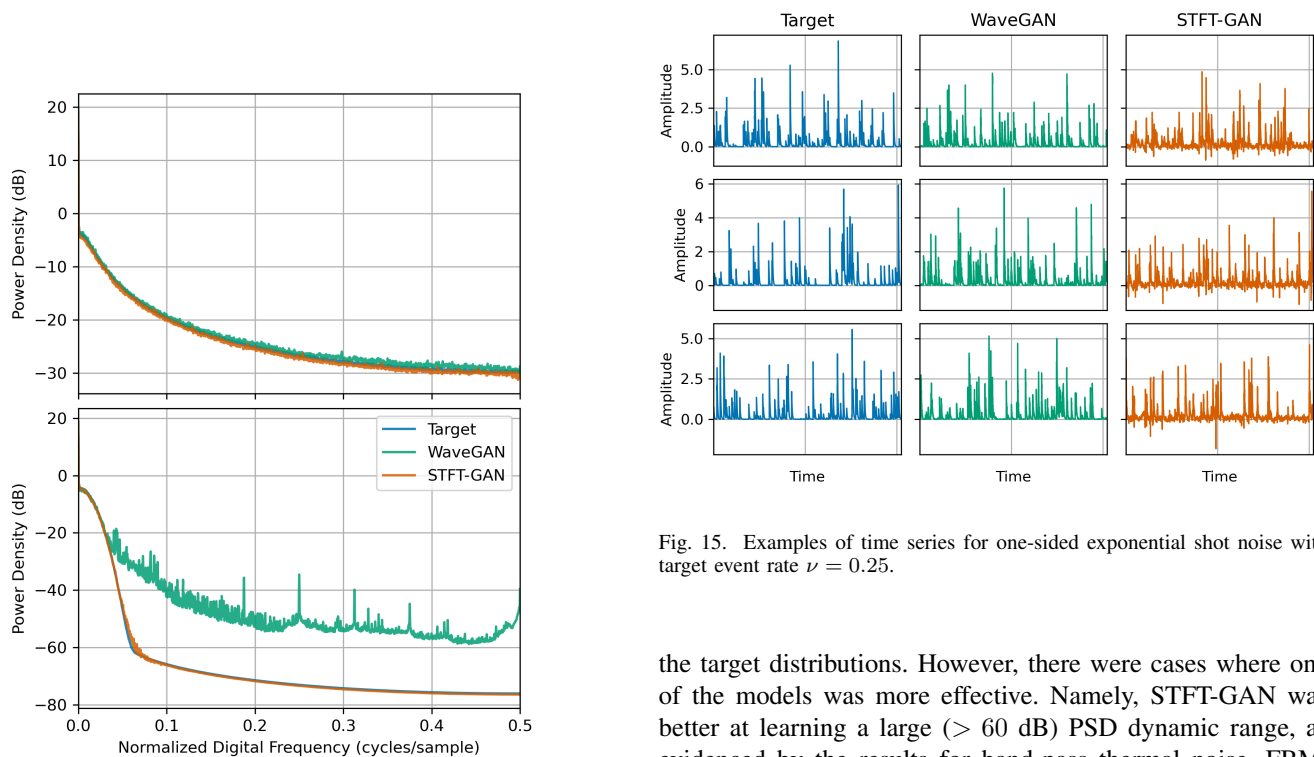


Fig. 15. Examples of time series for one-sided exponential shot noise with target event rate $\nu = 0.25$.

Fig. 14. Comparisons of median PSDs for Shot Noise with event rate $\nu = 1$. Top: One-sided exponential pulse type. Bottom: Gaussian pulse type.

the target distributions. However, there were cases where one of the models was more effective. Namely, STFT-GAN was better at learning a large (> 60 dB) PSD dynamic range, as evidenced by the results for band-pass thermal noise, FBM, and shot noise with the Gaussian pulse type; see Figures 9, 12, and 14. In addition, we found that the flexibility afforded by the choice of STFT dimension facilitated improvements in STFT performance, as shown by the FBM evaluations; see Figure 11. These findings indicate that the time-frequency

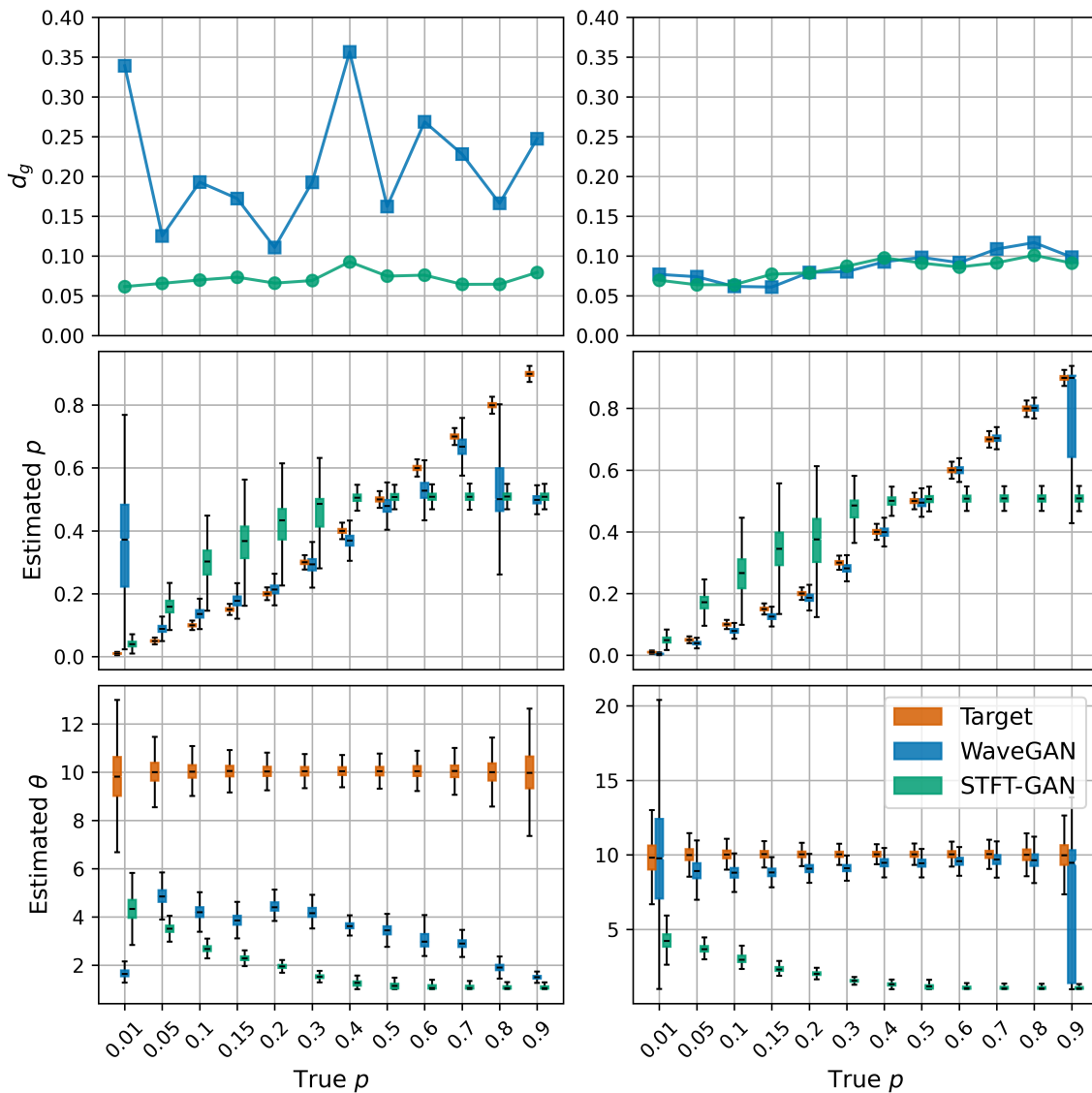


Fig. 16. Bernoulli-Gaussian noise results. Left Column: Baseline implementation. Right Column: With quantile data transformation. Top: Geodesic PSD distance plots. Middle: Boxplots of estimated impulse probability. Bottom: Boxplots of estimated scale parameter ratio.

STFT data representation, which more directly encodes the frequency content of a signal, facilitates learning spectral characteristics.

On the other hand, there was evidence that WaveGAN was more effective at learning time-domain signal characteristics, which are especially important for impulsive noise. For example, WaveGAN with the quantile data transformation accurately recovered the target impulsive BG noise distribution in most cases, whereas STFT-GAN did not; see Figure 16. Also, WaveGAN learned to correctly generate non-negative shot noise amplitudes; see Figure 15. These findings suggest that a hybrid GAN model combining both time-domain and frequency-domain features may be beneficial in some settings. This is an interesting topic for further research.

For the challenging case of non-Gaussian impulsive noise, we found that conventional GAN data preprocessing using feature min-max scaling was less effective than a quantile

data transformation that altered the data distribution in each channel to approximate a standard normal distribution. This outcome supports the hypothesis that conventional GANs are more adept at learning Gaussian data distributions.

Also, our findings with $S\alpha S$ noise indicate that the general-purpose GAN models evaluated here struggle with highly impulsive time series with extreme outliers. Further research into general-purpose GANs that can learn such time series is needed. There has been some recent work specifically focused on GANs for heavy-tailed distributions, e.g., [24], [91], [92], but it is unclear how well these approaches generalize.

The experimental evaluations presented here were necessarily limited in scope. Specifically, we did not attempt to evaluate all types of time series GANs or to propose a single GAN architecture that works optimally for all noise types. Moreover, we did not consider complex-valued noise, superpositions of multiple noise types, or time series with a deterministic

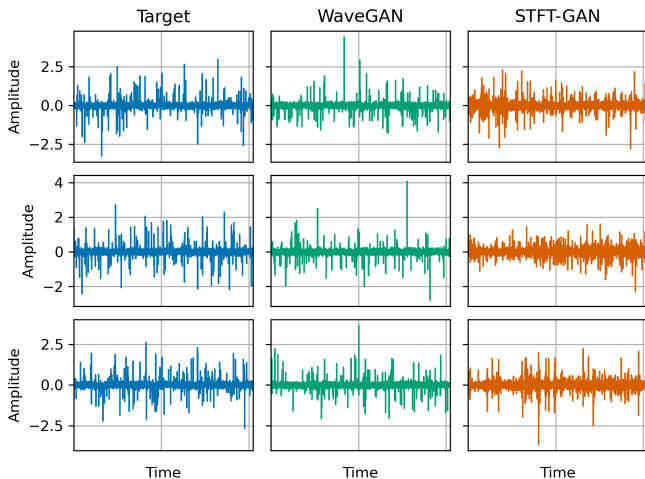


Fig. 17. Example time series for GANs trained on Bernoulli-Gaussian noise with quantile data transformation and target impulse probability, $p = 0.05$.

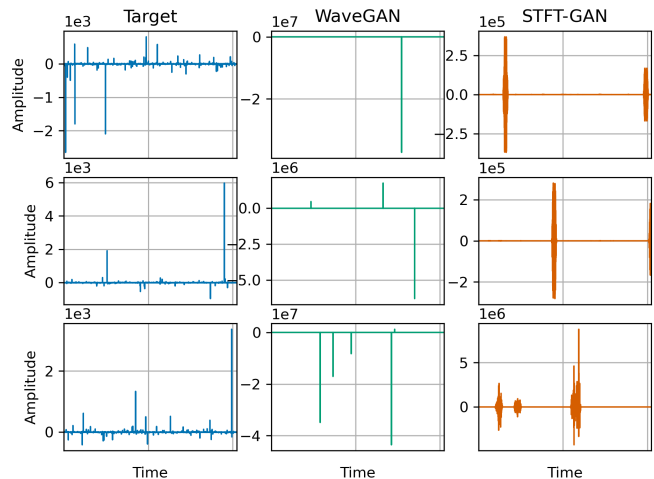


Fig. 19. Example time series for GANs trained on symmetric α -stable noise with quantile data transformation and target characteristic exponent, $\alpha = 1.0$.

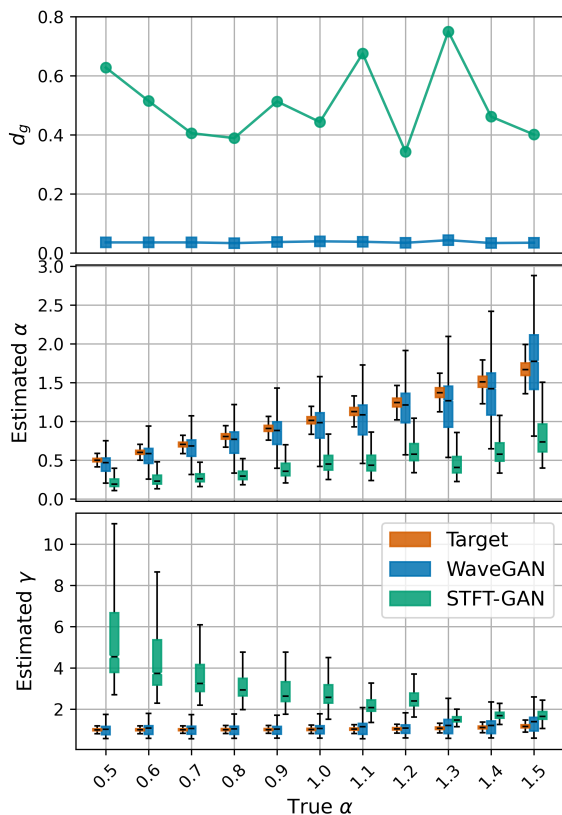


Fig. 18. Results for Symmetric α -stable noise with quantile data transformation. Top: Geodesic PSD distance plots. Middle: Boxplots of estimated characteristic exponent. Bottom: Boxplots of estimated scale parameter.

component. Evaluating the ability of deep generative models to learn these categories of random processes is of high interest for future studies.

In conclusion, our findings demonstrate that general-purpose time series GANs based on commonly-used deep convolutional architectures are capable of accurately learning many types of classical noise models, including Gaussian and non-

Gaussian distributions, as well as stationary and non-stationary random processes. These results give further evidence that GANs are a very promising class of generative models that can be applied to blindly learn a wide range of signal distributions. Moreover, our battery of tests with classical random processes provides a useful benchmark to aid further development of deep generative models for time series.

APPENDIX

EVENT RATE ESTIMATION FOR SHOT NOISE

We derive the event rate estimator given in equation (12) for the shot noise model of Section II-C under an exponential distribution for the pulse amplitudes. From classical results for filtered Poisson processes [4], [93], the mean and variance of of the shot noise process defined by Eq. (5) are

$$\mu_X = \nu E[A_n] I_1 \quad (13)$$

and

$$\sigma_X^2 = \nu E[A_n]^2 I_2, \quad (14)$$

respectively, where $E[\cdot]$ denotes mathematical expectation, $I_1 = \int_{-\infty}^{\infty} p(t) dt$, and $I_2 = \int_{-\infty}^{\infty} p(t)^2 dt$. Table I lists I_1 and I_2 for the three pulse functions considered here. Now, assuming that A_n follows an exponential distribution with mean β , it follows that $E[A_n] = \beta$ and $E[A_n^2] = 2\beta^2$. Thus, $\mu_X = \nu\beta I_1$ and $\sigma_X^2 = \nu(2\beta^2) I_2$. Solving the first equation for β , substituting the result into the second equation and solving for ν , we obtain

$$\nu = \frac{2\mu_X^2 I_2}{\sigma_X^2 I_1^2}. \quad (15)$$

Replacing μ_X and σ_X^2 by their sample estimates yields the estimator in Eq. (12). For the special case of a one-sided exponential pulse type, Eq. (15) is equivalent to Eq. (29) in [53] with $\epsilon = 0$.

REFERENCES

- [1] G. Vasilescu, *Electronic Noise and Interfering Signals: Principles and Applications*. Springer, 2006.
- [2] E. Milotti, *The Physics of Noise*. Morgan & Claypool Publishers, 2019.
- [3] H. H. Barrett and K. J. Myers, *Foundations of Image Science*. Hoboken, NJ: John Wiley & Sons, 2004.
- [4] R. M. Howard, *A Signal Theoretic Introduction to Random Processes*. Hoboken, NJ: John Wiley & Sons, 2016.
- [5] F. J. Montáns, F. Chinesta, R. Gómez-Bombarelli, and J. N. Kutz, “Data-driven modeling and learning in science and engineering,” *Comptes Rendus Mécanique*, vol. 347, no. 11, pp. 845–855, 2019.
- [6] D. Foster, *Generative Deep Learning: Teaching Machines to Paint, Write, Compose, and Play*. O’Reilly Media, 2019.
- [7] J. Langr and V. Bok, *GANs In Action: Deep learning with Generative Adversarial Networks*. Shelter Island, NY: Manning Publications, 2019.
- [8] S. Bond-Taylor, A. Leach, Y. Long, and C. G. Willcocks, “Deep generative modelling: A comparative review of VAEs, GANs, normalizing flows, energy-based and autoregressive models,” *IEEE Transactions on Pattern Analysis and Machine Intelligence*, 2021.
- [9] L. Ruthotto and E. Haber, “An introduction to deep generative modeling,” *GAMM-Mitteilungen*, vol. 44, no. 2, p. e202100008, 2021.
- [10] A. Creswell, T. White, V. Dumoulin, K. Arulkumaran, B. Sengupta, and A. A. Bharath, “Generative adversarial networks: An overview,” *IEEE Signal Processing Magazine*, vol. 35, no. 1, pp. 53–65, 2018.
- [11] Y. Hong, U. Hwang, J. Yoo, and S. Yoon, “How generative adversarial networks and their variants work: An overview,” *ACM Computing Surveys (CSUR)*, vol. 52, no. 1, pp. 1–43, 2019.
- [12] Z. Wang, Q. She, and T. E. Ward, “Generative adversarial networks in computer vision: A survey and taxonomy,” *ACM Computing Surveys (CSUR)*, vol. 54, no. 2, pp. 1–38, March 2022.
- [13] Z. Pan, W. Yu, X. Yi, A. Khan, F. Yuan, and Y. Zheng, “Recent progress on generative adversarial networks (GANs): A survey,” *IEEE Access*, vol. 7, pp. 36 322–36 333, 2019.
- [14] J. Chen, J. Chen, H. Chao, and M. Yang, “Image blind denoising with generative adversarial network based noise modeling,” in *Proceedings of the IEEE conference on computer vision and pattern recognition*, 2018, pp. 3155–3164.
- [15] J. M. Wolterink, T. Leiner, M. A. Viergever, and I. Išgum, “Generative adversarial networks for noise reduction in low-dose ct,” *IEEE transactions on medical imaging*, vol. 36, no. 12, pp. 2536–2545, 2017.
- [16] K. Lin, T. H. Li, S. Liu, and G. Li, “Real photographs denoising with noise domain adaptation and attentive generative adversarial network,” in *Proceedings of the IEEE/CVF Conference on Computer Vision and Pattern Recognition Workshops*, 2019, pp. 0–0.
- [17] Y. Ma, B. Wei, P. Feng, P. He, X. Guo, and G. Wang, “Low-dose CT image denoising using a generative adversarial network with a hybrid loss function for noise learning,” *IEEE Access*, vol. 8, pp. 67 519–67 529, 2020.
- [18] S. Cha, T. Park, B. Kim, J. Baek, and T. Moon, “GAN2GAN: Generative noise learning for blind denoising with single noisy images,” in *International Conference on Learning Representations*, 2021.
- [19] T. Zhang, J. Cheng, H. Fu, Z. Gu, Y. Xiao, K. Zhou, S. Gao, R. Zheng, and J. Liu, “Noise adaptation generative adversarial network for medical image analysis,” *IEEE Transactions on Medical Imaging*, vol. 39, no. 4, pp. 1149–1159, April 2020.
- [20] K. J. Miller and T. Du Bosq, “A machine learning approach to improving quality of atmospheric turbulence simulation,” in *Proc. SPIE, Infrared Imaging Systems: Design, Analysis, Modeling, and Testing XXXII*, vol. 11740, April 2021, p. 117400N.
- [21] Y. Zhou, Z. Zhu, X. Bai, D. Lischinski, D. Cohen-Or, and H. Huang, “Non-stationary texture synthesis by adversarial expansion,” *ACM Transactions on Graphics*, vol. 37, no. 4, pp. 1–13, 2018.
- [22] V. Mauduit, P. Abry, R. Leonarduzzi, S. G. Roux, and E. Quemener, “DCGAN for the synthesis of multivariate multifractal textures: How do we know it works?” in *2020 IEEE 30th International Workshop on Machine Learning for Signal Processing (MLSP)*. IEEE, 2020, pp. 1–6.
- [23] M. Baradad Jurjo, J. Wulff, T. Wang, P. Isola, and A. Torralba, “Learning to see by looking at noise,” *Advances in Neural Information Processing Systems*, vol. 34, pp. 2556–2569, 2021.
- [24] M. Zhou, J. Wang, X. Feng, H. Sun, J. Li, and X. Kuai, “On generative-adversarial-network-based underwater acoustic noise modeling,” *IEEE Transactions on Vehicular Technology*, vol. 70, no. 9, pp. 9555–9559, 2021.
- [25] C. Donahue, J. McAuley, and M. Puckette, “Adversarial audio synthesis,” in *International Conference on Learning Representations (ICLR)*, 2019, pp. 1–16. [Online]. Available: <https://arxiv.org/abs/1802.04208>
- [26] K. Kumar, R. Kumar, T. de Boissiere, L. Gestin, W. Z. Teoh, J. Sotelo, A. de Brébisson, Y. Bengio, and A. C. Courville, “MelGAN: Generative adversarial networks for conditional waveform synthesis,” in *Advances in Neural Information Processing Systems (NeurIPS 2019)*, vol. 32, 2019, pp. 1–12. [Online]. Available: <https://papers.nips.cc/paper/2019/file/6804c9bca0a615bdb9374d00a9fcb59-Paper.pdf>
- [27] K. E. Smith and A. O. Smith, “Conditional GAN for timeseries generation,” *arXiv:2006.16477*, 2020. [Online]. Available: <https://arxiv.org/abs/2006.16477>
- [28] J. Engel, K. K. Agrawal, S. Chen, I. Gulrajani, C. Donahue, and A. Roberts, “GANSynth: Adversarial neural audio synthesis,” in *International Conference on Learning Representations (ICLR)*, 2019, pp. 1–17. [Online]. Available: <https://arxiv.org/abs/1902.08710>
- [29] A. Marafioti, N. Perraudin, N. Holighaus, and P. Majdak, “Adversarial generation of time-frequency features with application in audio synthesis,” in *Proceedings of the 36th International Conference on Machine Learning (ICML)*, 2019, pp. 1–13. [Online]. Available: <http://proceedings.mlr.press/v97/marafioti19a/marafioti19a.pdf>
- [30] J. Nistal, S. Latner, and G. Richard, “Comparing representations for audio synthesis using generative adversarial networks,” in *28th European Signal Processing Conference (EUSIPCO)*, 2021, pp. 161–165.
- [31] C. Esteban, S. L. Hyland, and G. Rätsch, “Real-valued (medical) time series generation with recurrent conditional GANs,” *arXiv:1706.02633*, 2017. [Online]. Available: <https://arxiv.org/abs/1706.02633>
- [32] J. Yoon, D. Jarrett, and M. van der Schaar, “Time-series generative adversarial networks,” in *Advances in Neural Information Processing Systems (NeurIPS 2019)*, 2019, pp. 1–11. [Online]. Available: <https://papers.nips.cc/paper/2019/file/c9efe5f26cd17ba6216bbe2a7d26d490-Paper.pdf>
- [33] A. Radford, L. Metz, and S. Chintala, “Unsupervised representation learning with deep convolutional generative adversarial networks,” *arXiv*, 2015. [Online]. Available: <https://arxiv.org/abs/1511.06434>
- [34] M. Wiese, R. Knobloch, R. Korn, and P. Kretschmer, “Quant GANs: Deep generation of financial time series,” *Quantitative Finance*, vol. 20, no. 9, pp. 1419–1440, 2020.
- [35] J. Sklar and A. Wunderlich, “Feasibility of modeling orthogonal frequency-division multiplexing communication signals with unsupervised generative adversarial networks,” *Journal of Research of the National Institute of Standards and Technology*, vol. 126, pp. 1–25, 2021.
- [36] D. B. Percival and A. T. Walden, *Wavelet Methods for Time Series Analysis*. Cambridge, UK: Cambridge University Press, 2000.
- [37] A. Papoulis, *Probability, Random Variables, and Stochastic Processes*. New York: McGraw-Hill, 1965.
- [38] S. K. Mitra, *Digital Signal Processing: A Computer-Based Approach*, 2nd ed. New York: McGraw-Hill, 2001.
- [39] M. S. Keshner, “1/f Noise,” *Proceedings of the IEEE*, vol. 70, no. 3, pp. 212–218, 1982.
- [40] T. J. Rouphael, *Wireless Receiver Architectures and Design: Antennas, RF, synthesizers, mixed signal, and digital signal processing*. Academic Press, 2014.
- [41] J. R. Hosking, “Fractional differencing,” *Biometrika*, vol. 68, no. 1, pp. 165–176, 1981.
- [42] B. B. Mandelbrot and J. W. Van Ness, “Fractional Brownian motions, fractional noises and applications,” *SIAM Review*, vol. 10, no. 4, pp. 422–437, 1968.
- [43] J. Beran, Y. Feng, S. Ghosh, and R. Kulik, *Long-Memory Processes*. New York: Springer, 2013.
- [44] J. Veenstra, “Persistence and anti-persistence: Theory and software,” Ph.D. dissertation, University of Western Ontario, London, Ontario, Canada, 2013.
- [45] R. J. Barton and H. V. Poor, “Signal detection in fractional Gaussian noise,” *IEEE Transactions on Information Theory*, vol. 34, no. 5, pp. 943–959, 1988.
- [46] P. Flandrin, “On the spectrum of fractional Brownian motions,” *IEEE Transactions on Information Theory*, vol. 35, no. 1, pp. 197–199, 1989.
- [47] J. Q. Veenstra and A. I. McLeod, “arfima: Fractional ARIMA (and Other Long Memory) Time Series Modeling (version 1.7-0),” 2018. [Online]. Available: <https://cran.r-project.org/web/packages/arfima/>
- [48] A. I. McLeod, H. Yu, and Z. L. Krougly, “Algorithms for linear time series analysis: With R package,” *Journal of Statistical Software*, vol. 23, pp. 1–26, 2008.
- [49] E. Perrin, R. Harba, R. Jennane, and I. Iribarren, “Fast and exact synthesis for 1-D fractional Brownian motion and fractional Gaussian noises,” *IEEE Signal Processing Letters*, vol. 9, no. 11, pp. 382–384, 2002.

- [50] C. R. Dietrich and G. N. Newsam, "Fast and exact simulation of stationary gaussian processes through circulant embedding of the covariance matrix," *SIAM Journal on Scientific Computing*, vol. 18, no. 4, pp. 1088–1107, 1997.
- [51] E. Parzen, *Stochastic Processes*. San Francisco: Holden-Day, 1962.
- [52] D. L. Snyder and M. I. Miller, *Random Point Processes in Time and Space*, 2nd ed. New York: Springer, 1991.
- [53] A. Theodorsen, O. E. Garcia, and M. Rypdal, "Statistical properties of a filtered Poisson process with additive random noise: distributions, correlations and moment estimation," *Physica Scripta*, vol. 92, no. 5, p. 054002, 2017.
- [54] R. Pighi, M. Franceschini, G. Ferrari, and R. Raheli, "Fundamental performance limits of communications systems impaired by impulse noise," *IEEE Transactions on Communications*, vol. 57, no. 1, pp. 171–182, 2009.
- [55] G. A. Tsihrintzis and C. L. Nikias, "Performance of optimum and suboptimum receivers in the presence of impulsive noise modeled as an alpha-stable process," *IEEE Transactions on Communications*, vol. 43, no. 2/3/4, pp. 904–914, 1995.
- [56] M. Ghosh, "Analysis of the effect of impulse noise on multicarrier and single carrier QAM systems," *IEEE Transactions on Communications*, vol. 44, no. 2, pp. 145–147, 1996.
- [57] S. P. Herath, N. H. Tran, and T. Le-Ngoc, "On optimal input distribution and capacity limit of Bernoulli-Gaussian impulsive noise channels," in *2012 IEEE International Conference on Communications (ICC)*. IEEE, 2012, pp. 3429–3433.
- [58] K. L. Blackard, T. S. Rappaport, and C. W. Bostian, "Measurements and models of radio frequency impulsive noise for indoor wireless communications," *IEEE Journal on Selected Areas in Communications*, vol. 11, no. 7, pp. 991–1001, 1993.
- [59] M. Mirahmadi, A. Al-Dweik, and A. Shami, "BER reduction of OFDM based broadband communication systems over multipath channels with impulsive noise," *IEEE Transactions on Communications*, vol. 61, no. 11, pp. 4602–4615, 2013.
- [60] K. J. Kerpez and A. M. Gottlieb, "The error performance of digital subscriber lines in the presence of impulse noise," *IEEE Transactions on Communications*, vol. 43, no. 5, pp. 1902–1905, 1995.
- [61] I. Mann, S. McLaughlin, W. Henkel, R. Kirkby, and T. Kessler, "Impulse generation with appropriate amplitude, length, inter-arrival, and spectral characteristics," *IEEE Journal on Selected Areas in Communications*, vol. 20, no. 5, pp. 901–912, 2002.
- [62] H. Meng, Y. L. Guan, and S. Chen, "Modeling and analysis of noise effects on broadband power-line communications," *IEEE Transactions on Power Delivery*, vol. 20, no. 2, pp. 630–637, 2005.
- [63] V. Fernandes, W. A. Finamore, M. V. Ribeiro, N. Marina, and J. Karamachoski, "Bernoulli-Gaussian distribution with memory as a model for power line communication noise," in *Proc. Braz. Telecommun. Signal Process. Symp.*, 2017, pp. 328–332.
- [64] X. Kuai, H. Sun, S. Zhou, and E. Cheng, "Impulsive noise mitigation in underwater acoustic OFDM systems," *IEEE Transactions on Vehicular Technology*, vol. 65, no. 10, pp. 8190–8202, 2016.
- [65] J. Wang, J. Li, S. Yan, W. Shi, X. Yang, Y. Guo, and T. A. Gulliver, "A novel underwater acoustic signal denoising algorithm for Gaussian/non-Gaussian impulsive noise," *IEEE Transactions on Vehicular Technology*, vol. 70, no. 1, pp. 429–445, 2020.
- [66] T. Shongwe, A. H. Vinck, and H. C. Ferreira, "On impulse noise and its models," in *18th IEEE International Symposium on Power Line Communications and Its Applications*. IEEE, 2014, pp. 12–17.
- [67] J. P. Nolan, *Univariate Stable Distributions*. Cham, Switzerland: Springer, 2020.
- [68] C. L. Nikias and M. Shao, *Signal Processing with Alpha-Stable Distributions and Applications*. New York: John Wiley & Sons, 1995.
- [69] M. Shao and C. L. Nikias, "Signal processing with fractional lower order moments: stable processes and their applications," *Proceedings of the IEEE*, vol. 81, no. 7, pp. 986–1010, 1993.
- [70] P. G. Georgiou, P. Tsakalides, and C. Kyriakakis, "Alpha-stable modeling of noise and robust time-delay estimation in the presence of impulsive noise," *IEEE Transactions on Multimedia*, vol. 1, no. 3, pp. 291–301, 1999.
- [71] P. Harrison and J. M. Miotto, "PyLevy : Levy distributions for Python," 2020. [Online]. Available: <https://github.com/josemiotto/pylevy>
- [72] J. M. Chambers, C. L. Mallows, and B. Stuck, "A method for simulating stable random variables," *Journal of the American Statistical Association*, vol. 71, no. 354, pp. 340–344, 1976.
- [73] J. Nair, A. Wierman, and B. Zwart, *The Fundamentals of Heavy-Tails: Properties, Emergence, and Estimation*. Cambridge, UK: Cambridge University Press, July 2022, pre-publication version: <https://adamwierman.com/wp-content/uploads/2021/05/book-05-11.pdf>.
- [74] I. Goodfellow, Y. Bengio, A. Courville, and Y. Bengio, *Deep learning*. Cambridge, MA: MIT Press, 2016.
- [75] N. Ketkar and E. Santana, *Deep learning with Python*. New York: Springer, 2017.
- [76] J. O. Smith, *Spectral Audio Signal Processing*. Stanford, CA: W3K Publishing, 2011.
- [77] S. Mallat, *A Wavelet Tour of Signal Processing*, 3rd ed. San Diego, CA: Academic Press, 2009.
- [78] I. Gulrajani, F. Ahmed, M. Arjovsky, V. Dumoulin, and A. C. Courville, "Improved training of Wasserstein GANs," in *Advances in Neural Information Processing Systems (NeurIPS)*, 2017, pp. 1–11. [Online]. Available: <https://papers.nips.cc/paper/2017/file/892c3b1c6dcdd52936e27cbd0ff683d6-Paper.pdf>
- [79] D. P. Kingma and J. Ba, "Adam: A method for stochastic optimization," in *International Conference on Learning Representations (ICLR)*, 2015. [Online]. Available: <https://arxiv.org/abs/1412.6980>
- [80] A. DasGupta, *Fundamentals of Probability: A First Course*. New York: Springer, 2010.
- [81] F. Pedregosa, G. Varoquaux, A. Gramfort, V. Michel, B. Thirion, O. Grisel, M. Blondel, P. Prettenhofer, R. Weiss, V. Dubourg, J. Vanderplas, A. Passos, D. Cournapeau, M. Brucher, M. Perrot, and E. Duchesnay, "Scikit-learn: Machine learning in Python," *Journal of Machine Learning Research*, vol. 12, pp. 2825–2830, 2011.
- [82] D. J. Thomson, "Spectrum estimation and harmonic analysis," *Proceedings of the IEEE*, vol. 70, no. 9, pp. 1055–1096, 1982.
- [83] D. B. Percival and A. T. Walden, *Spectral Analysis for Univariate Time Series*. Cambridge, UK: Cambridge University Press, 2020.
- [84] T. Cokelaer and J. Hasch, "'Spectrum': Spectral Analysis in Python," *Journal of Open Source Software*, vol. 2, no. 18, p. 348, 2017.
- [85] T. T. Georgiou, "An intrinsic metric for power spectral density functions," *IEEE Signal Processing Letters*, vol. 14, no. 8, pp. 561–563, 2007.
- [86] —, "Distances between power spectral densities," *arXiv*, July 2006. [Online]. Available: <https://arxiv.org/abs/math/0607026>
- [87] J. Istas and G. Lang, "Quadratic variations and estimation of the local Hölder index of a Gaussian process," *Annales de l'Institut Henri Poincaré (B) Probability and Statistics*, vol. 33, no. 4, pp. 407–436, 1997.
- [88] J.-F. Coeurjolly, "Estimating the parameters of a fractional Brownian motion by discrete variations of its sample paths," *Statistical Inference for Stochastic Processes*, vol. 4, no. 2, pp. 199–227, 2001.
- [89] J.-F. Coeurjolly and E. Porcu, "Properties and Hurst exponent estimation of the circularly-symmetric fractional Brownian motion," *Statistics & Probability Letters*, vol. 128, pp. 21–27, 2017.
- [90] G. A. Tsihrintzis and C. L. Nikias, "Fast estimation of the parameters of alpha-stable impulsive interference," *IEEE Transactions on Signal Processing*, vol. 44, no. 6, pp. 1492–1503, 1996.
- [91] X. Zhang and J. Zhou, "A heavy-tailed distribution data generation method based on generative adversarial network," in *2021 IEEE 10th Data Driven Control and Learning Systems Conference (DDCLS)*. IEEE, 2021, pp. 535–540.
- [92] T. Huster, J. Cohen, Z. Lin, K. Chan, C. Kamhoua, N. O. Leslie, C.-Y. J. Chiang, and V. Sekar, "Pareto GAN: Extending the representational power of GANs to heavy-tailed distributions," in *International Conference on Machine Learning*, 2021, pp. 4523–4532.
- [93] R. L. Racicot, "Fitting a filtered Poisson process," *IMA Journal of Applied Mathematics*, vol. 7, no. 2, pp. 260–272, 1971.